



Vacancy-defect semiconductor quantum dots induced an S-scheme charge transfer pathway in 0D/2D structures under visible-light irradiation

Feng Bi^{a,1}, Yuetan Su^{a,1}, Yili Zhang^c, Meiling Chen^a, Jawwad A. Darr^d, Xiaole Weng^{a,b,*}, Zhongbiao Wu^a

^a Key Laboratory of Environment Remediation and Ecological Health, Ministry of Education, College of Environmental and Resource Sciences, Zhejiang University, 866 Yuhangtang Road, Hangzhou 310058, PR China

^b ZJU-Hangzhou Global Scientific and Technological Innovation Center, 311200 Hangzhou, PR China

^c Shanghai Municipal Engineering Design Institute Group Co., Ltd, 901 North Zhongshan (2nd) Road, Shanghai 200092, PR China

^d Christopher Ingold Laboratories, Department of Chemistry, University College London, 20 Gordon Street, London WC1H 0AJ, United Kingdom

ARTICLE INFO

Keywords:

S-scheme
Quantum dots
Defect
TiO₂
Photocatalysis

ABSTRACT

Designing heterojunctions with a feasible charge transfer pathway is a promising strategy for establishing highly efficient artificial photosystems. The step-scheme (S-scheme) heterojunction has shown considerable potential in enhancing redox ability and charge transfer of photocatalysts. Herein, a hierarchical heterojunction involving vacancy-defect TiO₂ quantum dots (QDs) and 2D g-C₃N₄ nanosheets was constructed using a multi-step assembly strategy. Computational and experimental studies show that the vacancy-defect TiO₂ QDs can induce an S-scheme charge transfer pathway in the 0D/2D heterojunction under visible-light irradiation, which greatly improved the redox ability of charge carriers, enhanced the charge transfer and separation at interfaces, and facilitated the H₂O adsorption and dissociation. This results in over 10-fold increase in hydrogen evolution reaction (HER) of photocatalytic water splitting for a wide range of carbon nitrides. The values achieved compare favorably with the best carbon nitride photocatalysts developed to date.

1. Introduction

Semiconductor quantum dots (QDs) are promising materials for establishing highly efficient artificial photosystems [1,2]. Comparing to their bulk counterparts, these materials can offer abundant surface uncoordinated sites for photochemical reaction, but exhibit unstable structure, higher recombination of photoinduced electrons and limited light response due to quantum confinement [3,4]. To overcome these shortcomings, semiconductor QDs are usually loaded on a two-dimensional (2D) host forming the hierarchical 0D/2D heterojunctions with inhibited self-aggregation and enhanced interfacial charge transfer, contributing to greatly increased photocatalytic

activities in H₂ production, CO₂ reduction and pollutant degradation [5–7].

Given the aforementioned benefits of 0D/2D heterojunctions, the materials still need to further improve redox ability and enhance charge migration efficiency for establishing highly efficient energy conversion and environmental control [8,9]. This demands their structures with a spatial distribution of reduction and oxidation potentials, and a matched band alignment in quantum-to-bulk hybrids. Amongst currently developed heterojunctions, an innovative step-scheme (S-scheme) heterojunction has been recently proposed by Yu et al. [10,11]. This heterojunction consists of two n-type semiconductors, with the reduction-type photocatalyst (RP) of more negative conduction band

Abbreviations: QDs, Quantum dots; NSs, Nanosheets; CHFS, Continuous hydrothermal flow system; sc-H₂O, Supercritical water; DFT, Density functional theory; EPR, Electron paramagnetic resonance; PALS, Positron annihilation lifetime spectroscopy; PL, Photoluminescence spectroscopy; TRPL, Time-resolved photoluminescence; EIS, Electrochemical impedance spectroscopy; HR-TEM, High resolution transmission electron microscopy; AFM, Atomic force microscopy; FFT, Fast Fourier transform; FT-IR, Fourier-transform infrared spectroscopy; TiBALD, Titanium(IV) bis(ammonium lactato)dihydroxide; TEOA, Triethanolamine; HER, Hydrogen evolution reaction; V_O, Oxygen vacancy.

* Corresponding author at: Key Laboratory of Environment Remediation and Ecological Health, Ministry of Education, College of Environmental and Resource Sciences, Zhejiang University, 866 Yuhangtang Road, Hangzhou 310058, PR China.

E-mail address: xlweng@zju.edu.cn (X. Weng).

¹ These authors contributed equally to this work.

<https://doi.org/10.1016/j.apcatb.2022.121109>

Received 2 December 2021; Received in revised form 26 December 2021; Accepted 15 January 2022

Available online 19 January 2022

0926-3373/© 2022 Elsevier B.V. All rights reserved.

(CB) position and oxidation-type photocatalyst (OP) of more positive valance band (VB) position. Under light irradiation, the photoelectrons and holes can accumulate separately at the lower VB and higher CB positions in the structure [11,12], which simultaneously ensures the stronger redox ability of photoinduced electrons and holes [13,14]. Consequently, by combining the benefits of 0D/2D and S-scheme heterojunctions, we can expect a novel 0D/2D S-scheme composite with excellent light harvesting capability, effective photogenerated electrons separation and transfer, and enhanced redox ability simultaneously [11, 12].

However, constructing such a 0D/2D S-scheme nanocomposite faces a challenge of how to precisely tune the band offsets acquired in the quantum-to-bulk hybrids. This usually requires the optimization on photochemical properties of semiconductor QDs, aiming to adjust the band alignment to match the 2D host. Difficulties can thus arise in terms of preserving the QD size and controlling their surface coordination environments during the optimization processing, as surface engineering of QDs generally needs harsh conditions [15,16], which can coarsen the QDs and destroy their surface chemistry. Moreover, despite the significant growth in the development of 0D/2D heterojunctions, the vast majority of QDs used to date are sulfides, vanadates and perovskites (e.g., CdS, Ag₂S, AgVO₃ and CsPbI₃) [5,17,18]. These QDs are either toxic to the environment due to the use of heavy metals or limited to large-scale production owing to their complex synthesis processes [19, 20], leading to the unfeasibility for industrial applications.

Based on the aforementioned issues, this work aims to shed light on three challenges for developing the innovative 0D/2D S-scheme heterojunction: (1) constructing an environmental-friendly 0D/2D heterojunction by using nontoxic semiconductor QDs and 2D host with a

matched band alignment; (2) developing a scalable approach for the manufacture and optimization of semiconductor QDs and their 0D/2D heterojunctions to meet industrial demands; (3) establishing an innovative 0D/2D S-scheme nanocomposite with the benefits of extended light harvesting (in particular visible-light), effective photogenerated electrons migration, and enhanced redox power simultaneously.

Firstly, we employed a continuous hydrothermal supercritical water (sc-H₂O) flow reactor (Fig. S1) [21] to manufacture the earth-abundant and environmental-friendly TiO₂ QDs. Such processes have been shown to deliver scalable and reproducible QD particles for a range of oxide materials (e.g., TiO₂, CeO₂, Co₃O₄, ZnO, NiO) [22]. The process is operated under high temperature (approximately 450 °C) and pressure (approximately 24.1 MPa), which can effectively preserve the QD size in the subsequent surface engineering. The obtained TiO₂ QDs bounded with lactate molecules owing to the use of titanium(IV) bis(ammonium lactato)dihydroxide (TiBALD) precursor [23,24], which was then loaded onto graphitic carbon nitride (g-C₃N₄) nanosheets under sonication (see Fig. 1a). In the final step, the composites were heat-treated in an inert N₂ atmosphere from 100 to 300 °C, which oxidized the bound lactate molecules and scavenged the labile O from the TiO₂ surface; this introduces abundant vacancy defects on the TiO₂ QDs surface. Subsequent computational and experimental studies confirmed that, the vacancy-defect TiO₂ QDs with a matched band alignment to g-C₃N₄, have induced an S-scheme charge transfer pathway within the heterojunction under visible illumination. This results in an over 10 times increase in photocatalytic hydrogen evolution rate (HER) from water for a great variety of carbon nitrides. The values achieved compare favorably with the best carbon nitride photocatalysts developed to date.

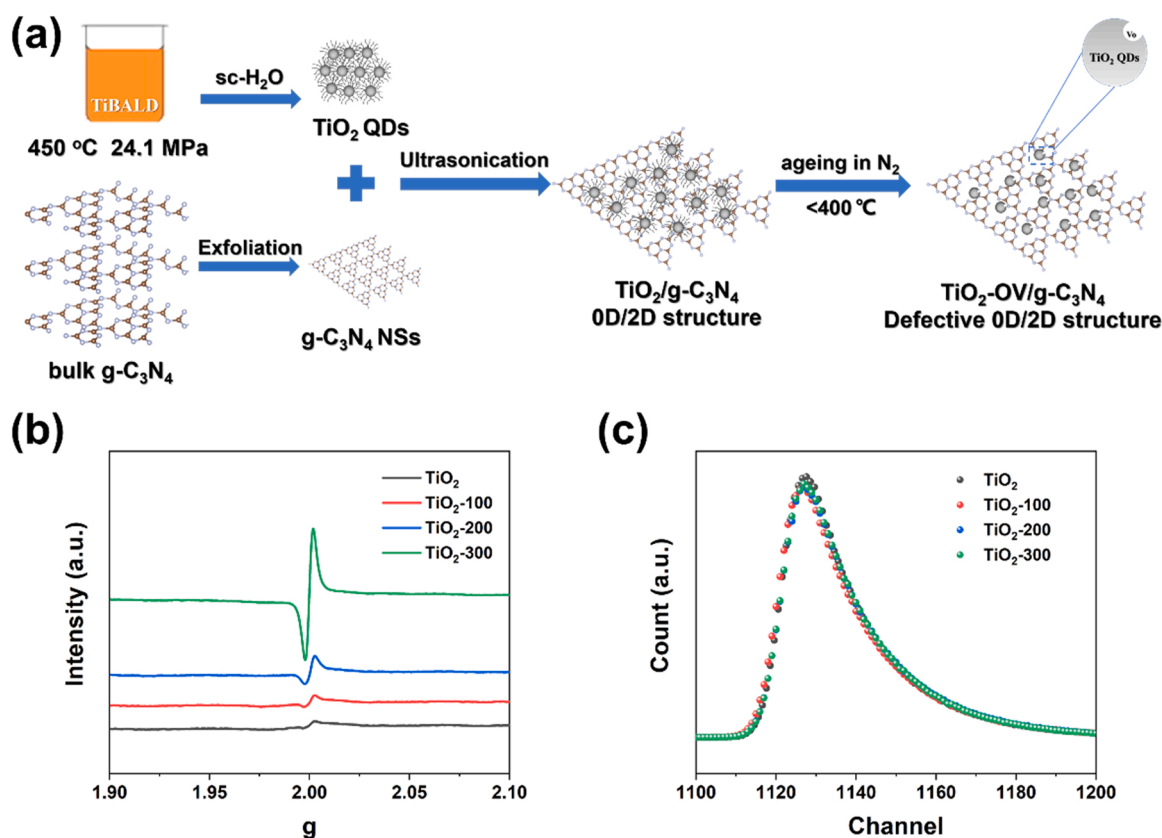


Fig. 1. (a) Schematic diagram for preparing the defective 0D/2D TiO₂-OV/g-C₃N₄ using a combined sc-H₂O route. (b) EPR and (c) positron lifetime spectra of TiO₂ QDs that were aged at different temperatures (100, 200 and 300 °C).

2. Experimental section

2.1. Fabrication of catalysts

2.1.1. Fabrication of vacancy-defect TiO₂ QDs

Ultrafine TiO₂ QDs were fabricated via a continuous hydrothermal flow system (CHFS, details are provided in [Supplementary Section S1](#), [Fig. S1](#)), as was reported in our previous work [24]. Defective TiO₂ QDs (denoted as TiO₂-OV) were obtained by further heating the pristine TiO₂ QDs under N₂ at different temperatures (100, 200, 300 °C) for 2 h, which were denoted as TiO₂-X (X represents the temperature).

2.1.2. Fabrication of g-C₃N₄ NSs

g-C₃N₄ nanosheets (NSs) were synthesized by an oxidation etching route using dicyandiamide as precursor [25,26]. The synthetic method was provided in the supplementary document.

2.1.3. Fabrication of defective TiO₂ QDs/g-C₃N₄ NSs

TiO₂ QDs/g-C₃N₄ NSs (denoted as TiO₂/g-C₃N₄) were fabricated using a multi-step assembly strategy. Especially, a certain amount (g) of TiO₂ QDs and 0.1 g g-C₃N₄ NSs were added into 40 mL distilled water, with the pH at approximately 6 according to their Zeta potential measurements (see [Fig. S2](#)). Subsequently, after ultrasonication for 40 min, the mixture was then centrifuged and washed with ultrapure water and ethanol, which was dried at 80 °C for 12 h to obtain the final products. TiO₂/g-C₃N₄ composites with different mass ratios (2:1, 1:1, 1:2, 1:3, and 1:4) were prepared by adjusting the added amounts of TiO₂. To fabricate defective TiO₂ QDs/g-C₃N₄ NSs (denoted as TiO₂-OV/g-C₃N₄) heterojunction, the TiO₂/g-C₃N₄ (1:2) were further heat-treated at different temperatures (100, 200, 300 °C) for 2 h under N₂ atmosphere (denoted as TiO₂/g-C₃N₄-X, X represents the temperature).

2.2. Characterization of catalysts

Details of characterization techniques, including X-ray diffraction (XRD), Fourier-transform infrared (FT-IR), transmission electron microscopy (TEM), atomic force microscope (AFM), UV-Vis diffuse reflection spectra (UV-Vis DRS), electron paramagnetic resonance (EPR), X-ray photoelectron spectroscopy (XPS), Kelvin probe force microscopy (KPFM), steady-state photoluminescence (PL), time-resolved photoluminescence (TRPL), and positron annihilation lifetime spectroscopy (PALS) are described in the [Supplementary Section S2–S3](#).

2.3. Photocatalytic and photoelectrochemical performance evaluation

Briefly, photocatalytic activities for hydrogen evolution were tested in a quartz reactor. Especially, the catalyst powders (50 mg) were added into 50 mL of 10 vol% triethanolamine (TEOA) aqueous solution. Before irradiation, the suspension was cleansed with Ar for 15 min to remove dissolved O₂ from the system. Then 1.2 wt% Pt as co-catalysts were in-situ photodeposited onto the surface of samples by photoreduction of H₂PtCl₆. Moreover, the testing temperature was maintained at 25 °C. The H₂ production properties were measured by Agilent 7890 A gas chromatograph (GC, Agilent, US), with Ar as the carrier gas. The Xe lamp (300 W, 400 nm cut-off filter, PLS-SXE300, Perfectlight, China) was served as the visible light source.

Additional details of photoelectrochemical measurements are available in [Supplementary Section S4](#).

2.4. Computational methods

Density functional theory (DFT) study was performed to investigate structural characteristics, charge density difference, Bader charge, molecule adsorption and Gibbs free energy using a VASP code [27]. The configuration was geometrically optimized to obtain the most stable adsorption configuration with the lowest energy. To understand the

adsorbate on the substrate catalyst, the adsorption energy (E_{ads}) was defined as:

$$E_{\text{ads}} = E_{\text{total}} - E_{\text{adsorbate}} - E_{\text{substrate}} \quad (1)$$

where E_{total} was total energy of the whole system after adsorption, and $E_{\text{adsorbate}}$ and $E_{\text{substrate}}$ represented the energies of the energies of the adsorbate and catalyst, respectively. A negative value corresponds to an exothermic process. Further details are shown in [Supplementary Section S5](#).

3. Results and discussion

3.1. Defective optimization of TiO₂ QDs

To preserve the TiO₂ QD size and uncoordinated surface during the manufacturing process, a continuous sc-H₂O flow synthesis process was employed to prepare TiO₂ QDs from a TiBALD water-soluble precursor; see [Supplementary data](#) for details of sc-H₂O syntheses and catalyst characterizations. Because the TiO₂ QDs were fabricated under a high temperature and pressure condition ($T = 450$ °C and $P_c = 24.1$ MPa), subsequent heat treatments can not coarsen the QDs. As demonstrated in [Fig. S3](#), up to 300 °C, nearly identical 3–10 nm TiO₂ QDs were preserved. Powder XRD ([Fig. S4–S6](#)) verified that the crystallite sizes of TiO₂ QDs were maintained at approximately 6.2 ± 0.2 nm (as calculated via Rietveld refinement) after the heat-treatments, with the lattice parameters preserved at $a = b = 3.79(1)$ Å and $c = 9.50(1)$ Å ([Table S1](#)).

After being subjected to low-temperature EPR and PALS, the relative concentration of oxygen vacancies on the TiO₂ QDs increased with the heat-treatment temperature (100–300 °C). The EPR spectra ([Fig. 1b](#)) contained an oxygen vacancies signal (i.e., $g = 2.002$) in TiO₂ anatase [28], whose intensity increased at higher temperatures. This indicated that more oxygen vacancies were formed owing to the efficient removal of surface lactate species at elevated temperatures. The PALS data ([Fig. 1c](#) and [Table S2](#)) yielded three lifetime components for the pristine and heat-treated TiO₂ QDs. The longest component (τ_3 , ca. 3.0–4 ns) was attributed to positron annihilation at interfaces [8,29], which accounted for <1% of the relative intensity. The shortest component (τ_1 , ca. 160–200 ps) corresponded to free annihilation of positrons in the defect-free crystal or that in small V_O [8,29], accounting for approximately 5–13% of the relative intensity. Another component (τ_2 , ca. 330–350 ps), accounting for approximately 87–95% of the relative intensity, originated from Ti³⁺-V_O associated with a large defect size [30]. In agreement with the EPR analyses, the dominant relative intensity (I_2), which can quantify the abundance of Ti³⁺-V_O, increased with heat-treatment temperature. These results further confirm that the relative concentration of V_O in the TiO₂ QDs could be readily tuned by adjusting the heat-treatment temperature.

3.2. Fabrication of vacancy-defect TiO₂ QDs/g-C₃N₄ heterojunction

To construct vacancy-defect TiO₂ QDs and g-C₃N₄ heterojunctions, the obtained TiO₂ from the sc-H₂O process was subsequently loaded onto exfoliated g-C₃N₄ NSs under ultrasonication, followed by heat-treatments in N₂ atmosphere from 100 to 300 °C. The 0D/2D heterojunction was analyzed via TEM ([Fig. 2a](#)) and AFM ([Fig. 2b](#)), yielding an average thickness of 4.0 nm (approximately 10 layers of g-C₃N₄ NSs). High-resolution TEM (HRTEM; [Fig. 2c–e](#)) further showed that, in the TiO₂-OV/g-C₃N₄ heterojunction, the spherical TiO₂-OV were confined to the g-C₃N₄ NSs with fringe intervals of 0.346 nm, which were assigned to TiO₂ anatase (101) lattice fringe, and the corresponding fast Fourier transform (FFT) pattern ([Fig. 2f](#)) suggested that the anatase particles were single crystals. FT-IR was used to evaluate the chemical structure and interaction of the obtained TiO₂/g-C₃N₄ heterojunction. The spectra for the heterojunction ([Fig. S7](#)) showed characteristic vibrations of both TiO₂ and g-C₃N₄, indicating proximal contact in their junctions. The

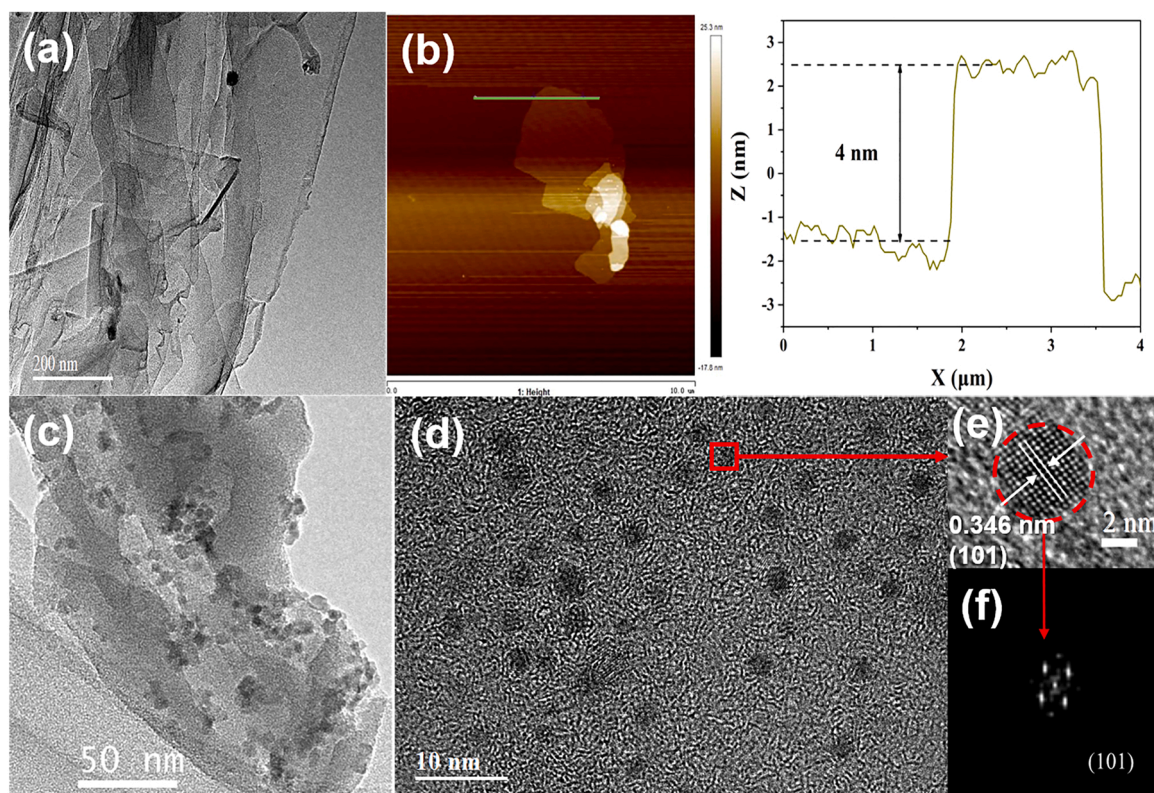


Fig. 2. (a) TEM and (b) AFM images of g-C₃N₄ NSs; (c) TEM and (d) HR-TEM image of TiO₂-OV/g-C₃N₄ heterojunction; (e) HR-TEM image and (f) corresponding FFT pattern of a single TiO₂ embedded on g-C₃N₄ and aged at 300 °C.

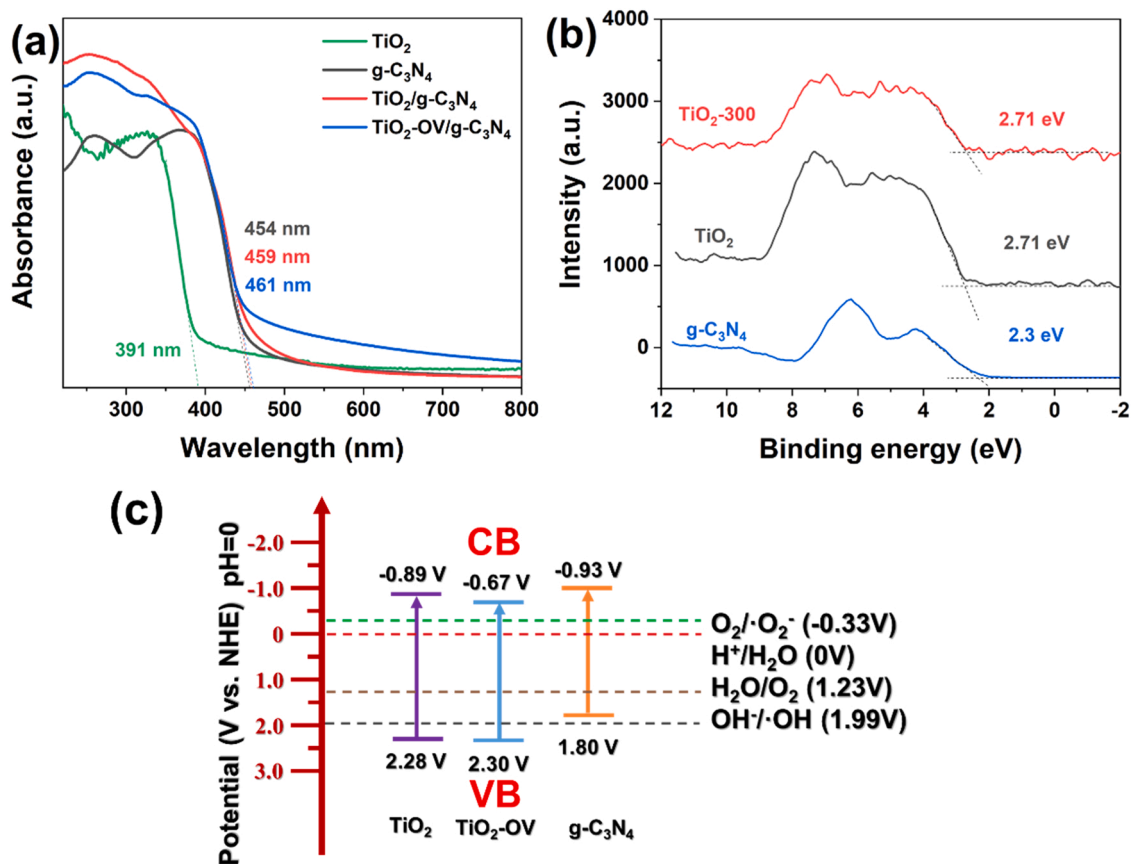


Fig. 3. (a) UV-Vis DRS spectra of g-C₃N₄ NSs, TiO₂/g-C₃N₄, and TiO₂-OV/g-C₃N₄. (b) VB-XPS spectra and (c) band structures of TiO₂, TiO₂-OV and g-C₃N₄.

slight shift of the N–H (3159 cm^{-1}) and Ti–O–Ti (503 cm^{-1}) bands for the composite suggested that the major interfacial interaction was between Ti 3d and N 2p orbitals, consistent with a previous report [31].

3.3. Confirmation of the S-scheme charge transfer pathway in OD/2D heterojunctions

To explore the internal charge transfer pathway amongst TiO_2 QDs, $\text{TiO}_2\text{-OV}$, and $\text{g-C}_3\text{N}_4$, their optical properties were first examined using UV-Vis DRS (Fig. 3a). The adsorption edge of TiO_2 QDs was measured at 391 nm with a band gap of 3.17 eV, indicating that this material is inactivation under visible-light illumination. Further ageing of the TiO_2 QDs from 100 to 300 °C exhibited a gradual red-shift in the UV-Vis DRS spectra (Fig. S8), and in particular, the TiO_2 QDs aged at 300 °C showed an adsorption edge at 418 nm with a corresponding bandgap energy of 2.97 eV, which is activated under visible illumination, and has been used in subsequent photochemical analyses (denoted as $\text{TiO}_2\text{-OV}$). In addition, the $\text{g-C}_3\text{N}_4$ exhibited a sharp adsorption edge at ca. 454 nm (bandgap, 2.73 eV), similar to a previous report [32].

On the basis of Mott–Schottky (M–S) plots, the flat-band potentials of TiO_2 QDs, $\text{TiO}_2\text{-OV}$, and $\text{g-C}_3\text{N}_4$ were calculated at -1.037 V , -1.018 V , and -1.109 V (vs. Ag/AgCl, pH = 7), respectively (Fig. S9), approximately equal to their Fermi levels in electrolytic solution [33]. The observed positive slope values of the straight part of M–S plots

indicate these materials are all n-type semiconductors [34]. To investigate their band structures, valance band X-ray photoelectron spectroscopy were performed (VB-XPS; Fig. 3b). Typically, for a semiconductor, the VB-XPS spectra correspond to the energy difference between VB position and the Fermi level [35,36]. Thus, by combining the Fermi levels and VB-XPS measurements (summarized in Table S3 and shown in Fig. 3c), the CB and VB positions of TiO_2 QDs were calculated at -0.89 and 2.28 V (vs. normal hydrogen electrode (NHE), pH = 0), those of $\text{TiO}_2\text{-OV}$ were at -0.67 and 2.30 V (vs. NHE, pH=0), and those of $\text{g-C}_3\text{N}_4$ were at -0.93 and 1.80 V (vs. NHE, pH=0).

To probe the transfer direction of photoinduced electrons between TiO_2 QDs, $\text{TiO}_2\text{-OV}$ and $\text{g-C}_3\text{N}_4$, their contact potential differences (CPD) were measured using KPFM [37]. As displayed in Fig. S10 and Table S4, the work functions of TiO_2 QDs, $\text{TiO}_2\text{-OV}$ and $\text{g-C}_3\text{N}_4$ were calculated at 4.91, 4.77, and 4.56 eV, respectively. This means the electrons will migrate from $\text{g-C}_3\text{N}_4$ to TiO_2 QDs and $\text{TiO}_2\text{-OV}$ upon contact without illumination.

The in situ irradiated XPS was further conducted to investigate the surface chemical states and photoinduced electrons migration over the photocatalysts. As displayed in Fig. 4a, the peaks at 284.8 and 287.9 eV in the C 1s XPS spectra are related to surface adventitious carbon species (C–C/C=C) and sp^2 -hybridized carbon in N=C–N aromatic rings, respectively [10,38,39]. These peaks in the $\text{TiO}_2\text{-OV/g-C}_3\text{N}_4$ heterojunction shifted toward higher binding energy (BE, ca. 288.2 eV) in

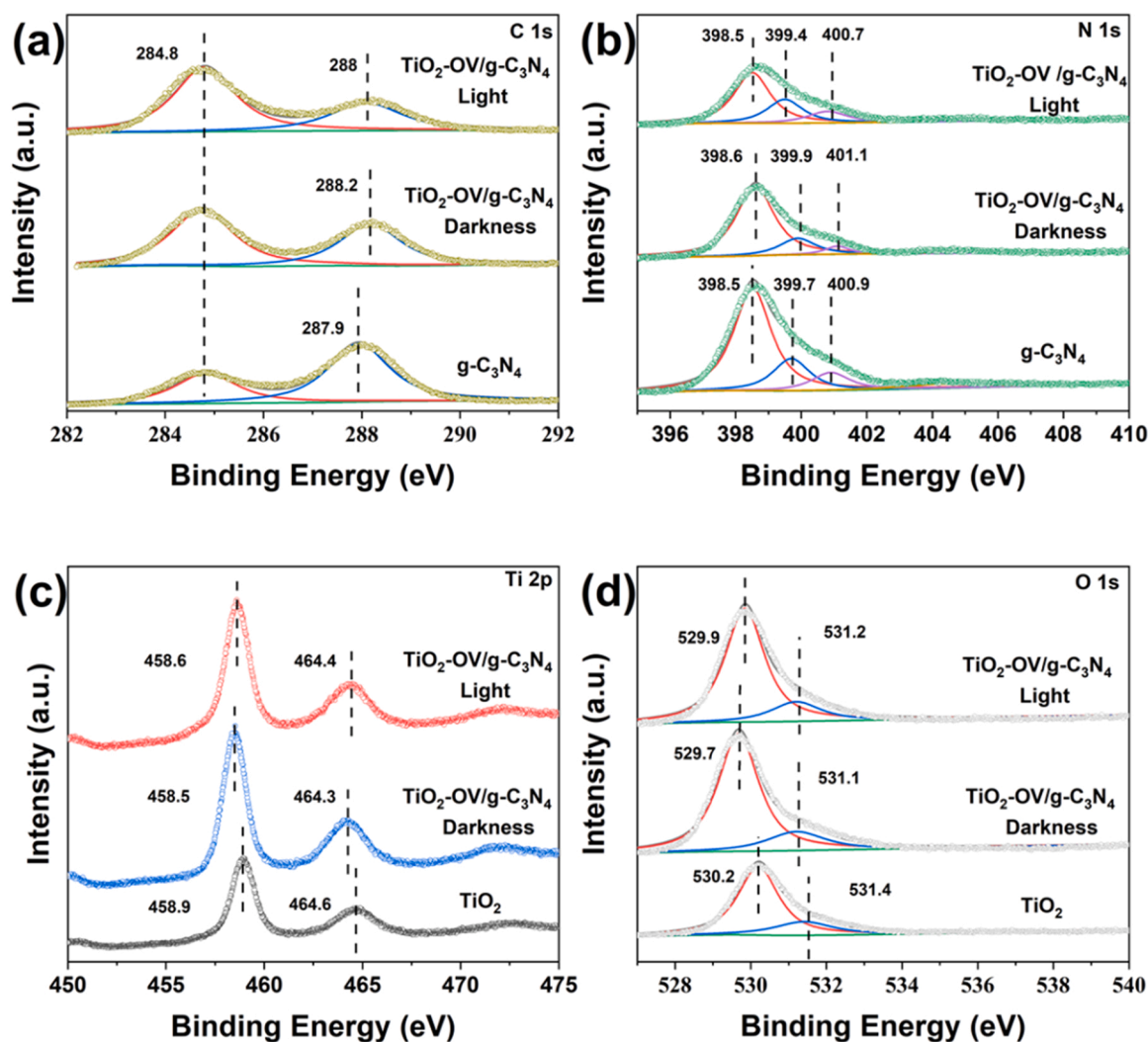


Fig. 4. High-resolution XPS spectra of (a) C 1s (b) N 1s (c) Ti 2p (d) O 1s for $\text{g-C}_3\text{N}_4$, TiO_2 and $\text{TiO}_2\text{-OV/g-C}_3\text{N}_4$ samples tested in darkness and under 365 nm LED illumination.

darkness and lower BE (ca. 288 eV) under illumination, suggesting that the g-C₃N₄ was an electron donor without illumination, consistent with the CPD analyses, but an electron acceptor under light irradiation. The N 1s XPS spectra show a similar electron migration phenomenon. As displayed in Fig. 4b, the typical peaks of N1s at 400.9, 399.7 and 398.5 eV correspond to surface amino N groups (N-H), three-coordinate N species (N-C)₃, and sp²-hybridized N atoms (C=N-C) in the triazine rings, respectively [10,38,39]. The BEs of the latter two N species shifted to higher range (N-C)₃: 399.9 eV; C=N-C: 398.6 eV) in darkness but lower range (N-C)₃: 399.4 eV; C=N-C: 398.4 eV) after light irradiation.

Additionally, to verify the electronic function of TiO₂-OV in the heterojunction, Ti 2p and O 1s XPS were measured. Two Ti 2p peaks at 458.9 and 464.6 eV (Fig. 4c) can be observed corresponding to Ti 2p_{3/2} and Ti 2p_{1/2}, respectively. Compared with TiO₂-OV, the BEs of Ti 2p (Ti 2p_{3/2}: 458.5 eV; Ti 2p_{1/2}: 464.3 eV) in TiO₂-OV/g-C₃N₄ composite obviously shifted to lower range in darkness, indicative of the TiO₂-OV as an electron acceptor without illumination. While under illumination, the BEs of Ti 2p (Ti 2p_{3/2}: 458.6 eV; Ti 2p_{1/2}: 464.4 eV) shifted to a higher range, suggesting the role of electron donor. Similarity, the O 1s XPS spectra exhibit two peaks at approximately 530.2 and 531.4 eV (Fig. 4d), corresponding to lattice oxygen (Ti-O) and surface-absorbed oxygen, respectively [38,40]. The BE of lattice oxygen shifted to lower range (529.7 eV) in darkness and higher range (529.9 eV) after illumination [10,38,39]. The XPS results indicate that in darkness, the photoexcited carriers migrate from g-C₃N₄ to TiO₂-OV, while the photoelectrons migrate from the TiO₂-OV to g-C₃N₄ (opposite direction) under illumination, resulting in the S-scheme charge transfer pathway across the OD/2D heterojunction.

EPR was further performed to demonstrate such an S-scheme pathway in the heterojunction under visible illumination. During the measurements, 5,5-dimethyl-1-pyrroline N-oxide (DMPO) was utilized to capture superoxide radicals ($\cdot\text{O}_2^-$) and hydroxyl radicals ($\cdot\text{OH}$) [41].

As displayed in Fig. 5a and b, under illumination, the TiO₂ QDs did not yield DMPO- $\cdot\text{O}_2^-$ and DMPO- $\cdot\text{OH}$ signals unsurprisingly, while for the TiO₂-OV, typical peaks of $\cdot\text{O}_2^-$ and $\cdot\text{OH}$ appeared, in good accordance with the UV-Vis DRS analyses (Fig. 3a). For the g-C₃N₄, DMPO- $\cdot\text{O}_2^-$ EPR signal was observed, but DMPO- $\cdot\text{OH}$ EPR signal was not detected, because the reason is that the CB position (-0.93 V vs. NHE, pH=0) of g-C₃N₄ was more negative than the potential of $\text{O}_2/\cdot\text{O}_2^-$ (-0.33 V vs. NHE, pH=0), and its VB position (1.80 V vs. NHE, pH=0) was less positive than the potential of $\text{OH}/\cdot\text{OH}$ (1.99 V vs. NHE, pH=0) [11,42]. Notably, after combining the TiO₂-OV and g-C₃N₄, both $\cdot\text{O}_2^-$ and $\cdot\text{OH}$ EPR signals were remarkably increased. This reveals that the OD/2D heterojunction has a strong redox capability with a separated distribution of reduction sites (g-C₃N₄) and oxidation sites (TiO₂-OV), and forms the S-scheme structure (Fig. 5c,d).

3.4. Photocatalytic activity measurements

To identify the benefits of vacancy-defect QDs and the S-scheme nature in the OD/2D composite, visible-light photocatalytic HER performances of catalysts were then investigated with TEOA as hole-scavenger. The HER value of pure g-C₃N₄ (Fig. 6a) was measured at approximately $104 \mu\text{mol g}^{-1} \text{h}^{-1}$, which is similar to that reported earlier [43]. With loading TiO₂ particles at different sizes, the HER rates gradually increased with reducing the TiO₂ size. The highest HER rate was obtained by loading the TiO₂ QDs at ca. 30 wt% (Fig. S11), which yielded a value of approximately $337 \mu\text{mol g}^{-1} \text{h}^{-1}$. Such an improvement with reducing TiO₂ particle size has been attributed to gradually accelerated charge transfer and separation in TiO₂-to-bulk hybrids [5]. As confirmed by our DFT calculation, reducing the TiO₂ size from Ti₂₄O₄₈ to Ti₈O₁₄ significantly increased the electron density at the OD/2D interfaces (Fig. 6c), and reduce the work function difference between TiO₂ and g-C₃N₄ (Fig. S12). The accumulation of net charges

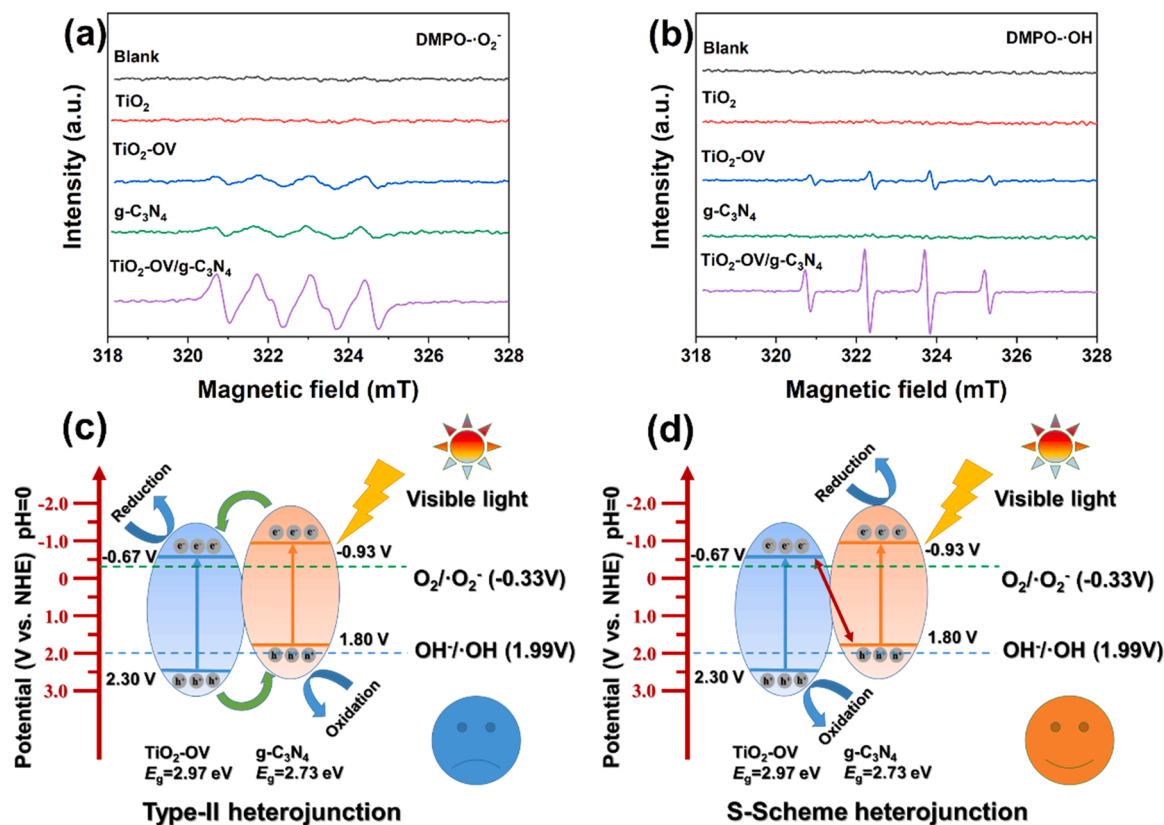


Fig. 5. EPR signals of (a) DMPO- $\cdot\text{O}_2^-$ in methanol dispersions and (b) DMPO- $\cdot\text{OH}$ in aqueous dispersions over various photocatalysts under visible light irradiation for 300 s. The schematic illustration of photogenerated charge carrier transfer in (c) type-II heterojunction and (d) S-scheme heterojunction.

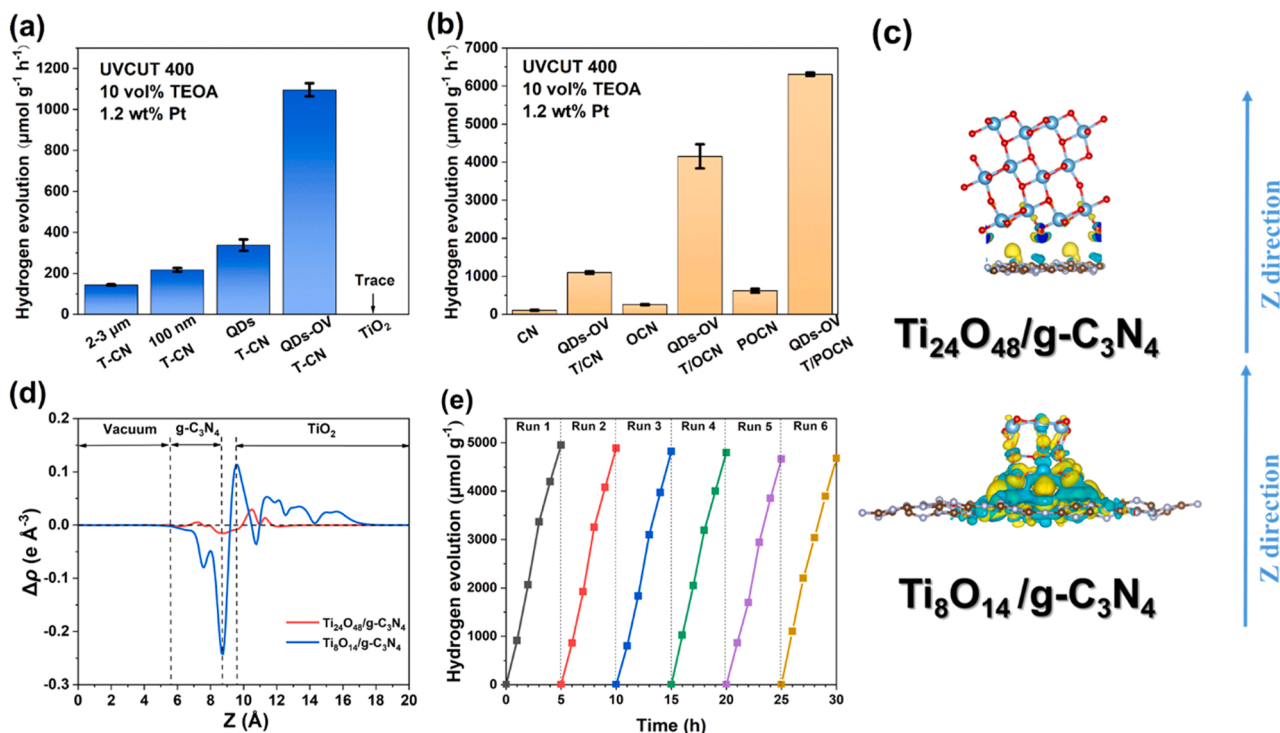


Fig. 6. (a–b) Photocatalytic activities of different photocatalysts for H_2 evolution under visible light illumination ($\lambda \geq 400$ nm, 10 vol% TEOA as scavenger and 1.2 wt% H_2PtCl_6 as co-catalyst). (c) Charge density difference and (d) planar-averaged charge density difference along the Z direction of $\text{Ti}_{24}\text{O}_{48}/\text{g-C}_3\text{N}_4$ NSs and $\text{Ti}_8\text{O}_{14}/\text{g-C}_3\text{N}_4$ NSs (Charge accumulation is shown in yellow and charge depletion is labeled in blue, with an iso-value of $0.001 \text{ e} \text{\AA}^{-3}$. Brown, light blue, blue and red spheres represent C, N, Ti, O atoms, respectively). (e) Cycling runs for photocatalytic activities on the $\text{TiO}_2\text{-OV}/\text{g-C}_3\text{N}_4$ heterojunction (aged at 300°C).

between the $\text{Ti}_8\text{O}_{14}/\text{g-C}_3\text{N}_4$ interfaces induced a strong internal electric field, greatly enhancing the charge separation and transfer in the 0D/2D heterojunction. Furthermore, the planar-average charge density difference along the Z direction (Fig. 6d) proposes that electrons between the $\text{Ti}_8\text{O}_{14}/\text{g-C}_3\text{N}_4$ interfaces mainly migrated from $\text{g-C}_3\text{N}_4$ to TiO_2 QDs without illumination, consistent with the CPD and XPS results (Fig. 4 and Fig. S10).

Following the preparation of $\text{TiO}_2\text{-OV}/\text{g-C}_3\text{N}_4$ heterojunction that were heat-treated as a final step at temperatures in the range $100\text{--}300^\circ\text{C}$, all samples exhibited improved HER performances compared with pure $\text{g-C}_3\text{N}_4$ (Fig. S13). The 100 and 200°C aged samples exhibited relatively similar HER rates to TiO_2 QDs/ $\text{g-C}_3\text{N}_4$ heterojunction, because of their $\text{TiO}_2\text{-OV}$ inactivation under visible illumination (Fig. S8), while the 300°C -aged sample with an adsorption edge at 461 nm (see Fig. 3a) has yielded a HER rate of approximately $1096 \mu\text{mol g}^{-1} \text{h}^{-1}$, nearly 10-fold higher than $\text{g-C}_3\text{N}_4$. Notably, such an improvement is universal for a great variety of carbon nitrides, as by using the P- and O-modified $\text{g-C}_3\text{N}_4$ as a 2D host, the HER rate of the 0D/2D heterojunction can be further increased to approximately $6308 \mu\text{mol g}^{-1} \text{h}^{-1}$ (see Fig. 6b), competing with the best reported carbon nitride photocatalysts to date (Table S5) [32,44,45].

In addition, the 0D/2D S-scheme heterojunction also showed a high oxidation ability in photocatalytic degradation of rhodamine B. As displayed in Fig. S14 and Table S6, after irradiation for 60 min, nearly 100% rhodamine B ($k_a=0.0603$) has been degraded over the $\text{TiO}_2\text{-OV}/\text{g-C}_3\text{N}_4$ heterojunction. Its reaction rate is approximately 7 times that of the pristine $\text{g-C}_3\text{N}_4$ (63% , $k_a=0.0085$). The stability of $\text{TiO}_2\text{-OV}/\text{g-C}_3\text{N}_4$ heterojunction was also estimated by performing six reaction cycles with intermittent evacuation and re-loading of TEOA to compensate for any losses after each run. As displayed in Fig. 6e and Supplementary Fig. S15–S17, the cumulative H_2 evolution did not show obvious decrease in repeated runs, and the XRD, XPS, and FT-IR measurements on its textual properties did not show noticeable change after photocatalytic reaction, revealing a high photocatalytic stability of $\text{TiO}_2\text{-OV}/$

$\text{g-C}_3\text{N}_4$ heterojunction.

Transfer kinetics of photoelectrons in the as-prepared samples were also investigated by using PL, TRPL, and electrochemical measurements. The PL spectra (see Fig. S18) revealed both the $\text{TiO}_2/\text{g-C}_3\text{N}_4$ and $\text{TiO}_2\text{-OV}/\text{g-C}_3\text{N}_4$ displayed largely weakened emission signals compared with $\text{g-C}_3\text{N}_4$, which is owing to their considerably inhibited recombination rate and increased separation rate of photogenerated electrons at interfaces [46]. The TRPL decay spectra (see Fig. S19) estimated based on a double-exponential decay [47] shows that the intensity-average lifetimes ($\langle \tau \rangle$) of emission decay was calculated at 4.45, 3.12, and 2.82 ns for $\text{g-C}_3\text{N}_4$, $\text{TiO}_2/\text{g-C}_3\text{N}_4$ and $\text{TiO}_2\text{-OV}/\text{g-C}_3\text{N}_4$, respectively (see Table S7 and Section S6). The shortest lifetime in the $\text{TiO}_2\text{-OV}/\text{g-C}_3\text{N}_4$ heterojunction implies that defect engineering further enhances charge transfer at the 0D/2D interfaces [48]. The charge separation and recombination were determined by electrochemical impedance spectroscopy (EIS) characterization, which were presented in the form of Nyquist plots. The Nyquist plots in the EIS are displayed in Fig. S20, where a smaller diameter suggests a faster rate of electron–hole separation and smaller charge transfer resistance [48]. $\text{TiO}_2\text{-OV}/\text{g-C}_3\text{N}_4$ had the smallest arc radius among all samples, indicating that it had the smallest charge transfer resistance and the defect engineering has also enhanced the photogenerated charge separation.

3.5. Reaction mechanism analyses

After identifying the function of vacancy-defect TiO_2 QDs for inducing S-scheme mechanism in the 0D/2D heterojunction, further investigations were performed to evaluate its reaction mechanism in photocatalytic H_2 evolution. In general, under an alkaline environment, the photocatalytic H_2 generation from water generally follows a four-step process when the TEOA is used as the sacrificial agent [10].

Step 1: $\text{H}_2\text{O} + * \rightarrow \text{H}_2\text{O}^*$

Step 2: $\text{H}_2\text{O}^* + * \rightarrow \text{H}^* + \text{OH}^*$ (Volmer step)

Step 3: $\text{OH}^* + \text{e}^- \rightarrow \text{OH}^- + *$

$\text{H}^* + \text{H}_2\text{O}^* \rightarrow \text{H}_2^* + \text{OH}^*$ (Heyrovsky step)

$\text{H}^* + \text{H}^* \rightarrow \text{H}_2^*$ (Tafel step)

Step 4: $\text{H}_2^* \rightarrow \text{H}_2(\text{g}) + *$

where the adsorption and dissociation of H_2O molecules into H and OH groups on the semiconductor surface is an initial step (Volmer step), followed by the reaction between dissociated H^* protons (Tafel step) or those with adsorbed H_2O^* (Heyrovsky step) to form H_2^* . The Volmer step is believed to be a rate-determining step, as either the Heyrovsky or Tafel step will be considerably accelerated over the Pt co-catalyst. This was verified by the fact that removing H_2PtCl_6 caused both the $\text{TiO}_2/\text{g-C}_3\text{N}_4$ and $\text{TiO}_2\text{-OV}/\text{g-C}_3\text{N}_4$ heterojunctions exhibiting poor HER performance under visible-light irradiation. Accordingly, our DFT calculations only considered the energetic favorability of the Volmer step in photocatalytic water splitting.

A model of platinum cluster (Pt_4) supported on the $\text{TiO}_2/\text{g-C}_3\text{N}_4$ system was constructed according to previous reports [49]. By comparing the adsorption energies of the Pt_4 cluster at different locations on $\text{TiO}_2/\text{g-C}_3\text{N}_4$ (namely $\text{Ti}_8\text{O}_{14}/\text{g-C}_3\text{N}_4$) and $\text{TiO}_2\text{-OV}/\text{g-C}_3\text{N}_4$ (namely $\text{Ti}_8\text{O}_{13}/\text{g-C}_3\text{N}_4$) heterojunctions (Fig. S21 and Table S8-S9), it was noted that the Pt_4 clusters tended to attach at the interface in both structures, which yielded the adsorption energies of -6.28 eV and -6.32 eV, respectively. Given the accumulation of photogenerated net charges at the interface of OD/2D heterojunction (see Fig. 6c), locating the Pt co-catalyst nearby the interface is expected to greatly facilitate the photochemical reaction (see Fig. 6a,b).

In the Volmer reaction, H_2O was shown to preferentially adsorb near the Pt_4 cluster on $\text{Ti}_8\text{O}_{14}/\text{g-C}_3\text{N}_4$ heterojunction, with an adsorption energy of -0.91 eV (Fig. 7a). The adsorbed H_2O is then dissociated into OH^* and H^* , with OH bound to the Pt site and H migrating to the neighboring O site. This step is exothermic by 0.81 eV, with an energy barrier of 0.10 eV. The Bader charge calculation (see Fig. 7b) shows only 0.14 e charge transfer from the $\text{Ti}_8\text{O}_{14}/\text{g-C}_3\text{N}_4$ to adsorbed H_2O . In comparison, the $\text{Ti}_8\text{O}_{13}/\text{g-C}_3\text{N}_4$ heterojunction exhibits an H_2O adsorption energy of 1.62 eV, which is considerably higher than that of the $\text{Ti}_8\text{O}_{14}/\text{g-C}_3\text{N}_4$ heterojunction, suggesting that defect engineering can further enhance the H_2O adsorption on the OD/2D heterojunction. Notably, the adsorbed H_2O on the $\text{Ti}_8\text{O}_{13}/\text{g-C}_3\text{N}_4$ heterojunction spontaneously dissociates into OH^* without energy barrier, and compared with $\text{Ti}_8\text{O}_{14}/\text{g-C}_3\text{N}_4$ heterojunction, the Bader charge calculation shows a much higher charge transfer (0.34 e) on $\text{Ti}_8\text{O}_{13}/\text{g-C}_3\text{N}_4$ heterojunction. The DFT calculations indicate defect engineering effectively enhances the H_2O adsorption and dissociation on $\text{Pt}/\text{Ti}_8\text{O}_{13}/\text{g-C}_3\text{N}_4$ surface, and the Volmer reaction is more favorable on $\text{Ti}_8\text{O}_{13}/\text{g-C}_3\text{N}_4$ heterojunction than $\text{Ti}_8\text{O}_{14}/\text{g-C}_3\text{N}_4$. Furthermore, FT-IR (Fig. 7c) and EPR analyses (Fig. 7d) confirmed that the $\text{TiO}_2\text{-OV}/\text{g-C}_3\text{N}_4$ heterojunction yielded more intense vibration at approximately 3500 cm^{-1} (surface hydroxyl groups) [50,51] after introducing saturated H_2O , and exhibited increased EPR signal for $\text{DMPO}\cdot\text{OH}$ after irradiation, both of which are in agreement with the DFT calculations.

4. Conclusions

An innovative vacancy-defect OD/2D S-scheme heterojunction was successfully designed and constructed using a multistep assembly

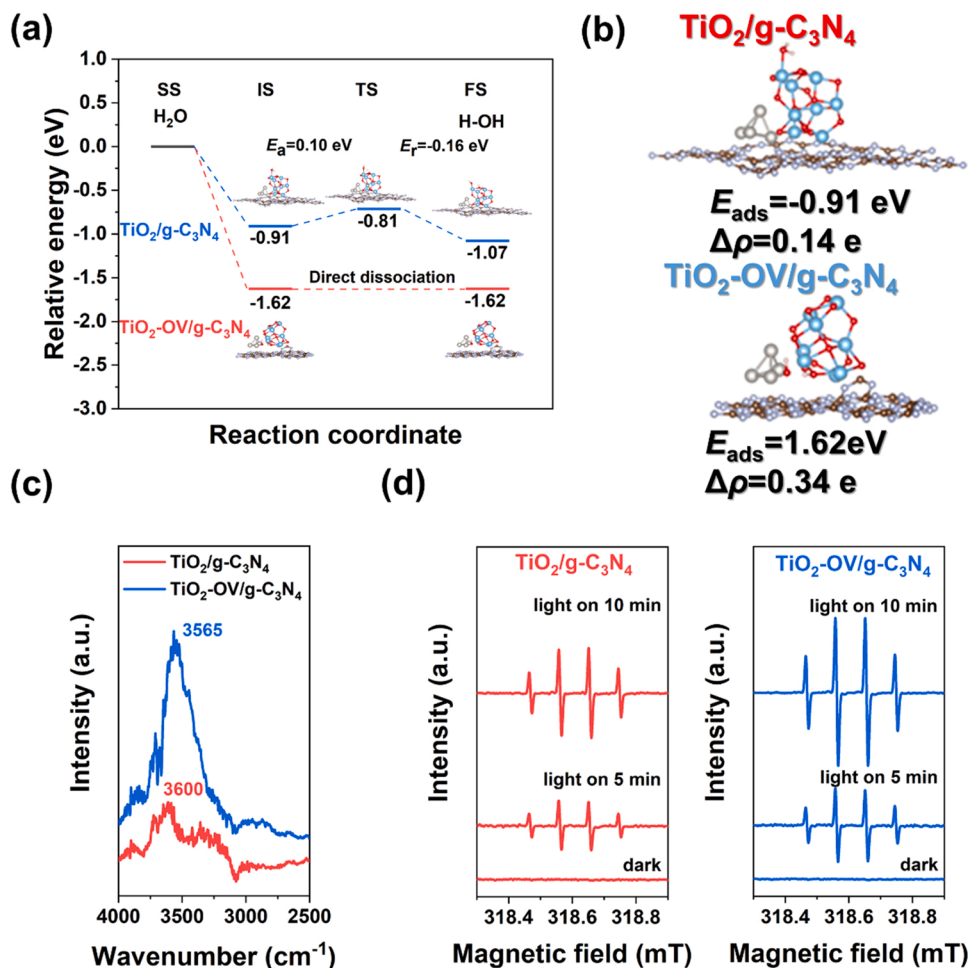


Fig. 7. (a) Adsorption and reaction pathway of H_2O molecules on the $\text{TiO}_2/\text{g-C}_3\text{N}_4$ and $\text{TiO}_2\text{-OV}/\text{g-C}_3\text{N}_4$ (heat-treated at 300°C) surface. “SS”, “IS”, “TS” and “FS” stand for the separate state, the initial state, the transition state, and the final state, respectively. The reference energy is that of the separate states. (b) Optimized geometric structure of H_2O molecules adsorption on $\text{TiO}_2/\text{g-C}_3\text{N}_4$ and $\text{TiO}_2\text{-OV}/\text{g-C}_3\text{N}_4$. E_{ads} is the adsorption energy of H_2O molecules. $\Delta\rho$ is the Bader charge change of the adsorbed H_2O , and positive values refer to the transportation of charge carriers from the catalyst surface to the adsorbed H_2O . (c) H_2O FT-IR spectra. (d) EPR spectra of the $\text{DMPO}\cdot\text{OH}$ radicals.

strategy. As part of this process, a highly scalable continuous supercritical water flow reactor was employed for the synthesis of semiconductor QDs. Importantly, this synthetic route yielded TiO₂ QDs with abundant surface oxygen vacancies without changing the QD size. KPFM, in situ irradiated XPS, EPR measurements, and theoretical calculations provided strong evidence to confirm the S-scheme migration in the TiO₂-OV/g-C₃N₄ heterojunction, and indicated that the vacancy-defect 0D/2D S-scheme heterojunction has strong redox ability, superior interfacial charge separation and transfer efficiency, and barrierless H₂O dissociation ability, which essentially improves the photocatalytic hydrogen evolution under visible illumination. This study provides a perspective for manufacturing and optimizing vacancy-defect 0D/2D S-scheme heterojunctions. Mapping to the future, given the scalability for the QD continuous hydrothermal synthesis process (including a pilot scale facility in the lab of one of the co-authors and the potentiality of 1000 Ton nanoparticles (NPs) per year by the Hanwha Corporation facility [22]), it should be possible to perform large-scale production of defective semiconductor QDs and the corresponding 0D/2D composites. This will form part of our future endeavors which will be reported in due course.

CRedit authorship contribution statement

Xiaole Weng conceived and led the studies. Feng Bi performed experiments, data analyses and wrote the first draft of paper. Yuetan Su conducted DFT calculations. Yili Zhang and Meiling Chen performed catalyst characterizations. Jawwad A. Darr and Zhongbiao Wu discussed the results and commented on the manuscript.

Declaration of Competing Interest

The authors declare that they have no known competing financial interests or personal relationships that could have appeared to influence the work reported in this paper.

Acknowledgements

This work was supported by the National Natural Science Foundation of China (21922607, 51878598), the Outstanding Youth Project of Zhejiang Natural Science Foundation (LR19E080004) and Key special project of "Science and Technology Helps Economy 2020" (2020ZLHJ01-4). The authors also wanted to acknowledge Prof. Jiaguo Yu (Wuhan University of Technology) for the help on in situ irradiated XPS measurements, Shiyanjia Lab (www.shiyanjia.com) for the support of KPFM tests and Perfectlight for the assistance of photocatalytic performance tests. JAD was supported by the JUICED energy hub (EPSRC reference EP/R023662/1).

Supporting Information

Experimental section, schematic diagram, TEM, XRD Rietveld refinement, FT-IR, XPS, UV-Vis DRS, MS plots, CPDs, PALS, PL, TRPL, EIS, band structure, DFT calculations and additional figures for experimental and calculated results.

Appendix A. Supporting information

Supplementary data associated with this article can be found in the online version at [doi:10.1016/j.apcatb.2022.121109](https://doi.org/10.1016/j.apcatb.2022.121109).

References

- [1] X.-B. Li, C.-H. Tung, L.-Z. Wu, Semiconducting quantum dots for artificial photosynthesis, *Nat. Rev. Chem.* 2 (2018) 160–173.
- [2] S. Kundu, A. Patra, Nanoscale strategies for light harvesting, *Chem. Rev.* 117 (2017) 712–757.

- [3] G.H. Carey, A.L. Abdelhady, Z. Ning, S.M. Thon, O.M. Bakr, E.H. Sargent, Colloidal quantum dot solar cells, *Chem. Rev.* 115 (2015) 12732–12763.
- [4] R.S. Selinsky, Q. Ding, M.S. Faber, J.C. Wright, S. Jin, Quantum dot nanoscale heterostructures for solar energy conversion, *Chem. Soc. Rev.* 42 (2013) 2963–2985.
- [5] M.Y. Ye, Z.H. Zhao, Z.F. Hu, L.Q. Liu, H.M. Ji, Z.R. Shen, T.Y. Ma, 0D/2D heterojunctions of vanadate quantum dots/graphitic carbon nitride nanosheets for enhanced visible-light-driven photocatalysis, *Angew. Chem. Int. Ed.* 56 (2017) 8407–8411.
- [6] D.L. Huang, Z.H. Li, G.M. Zeng, C.Y. Zhou, W.J. Xue, X.M. Gong, X.L. Yan, S. Chen, W.J. Wang, M. Cheng, Megamerger in photocatalytic field: 2D g-C₃N₄ nanosheets serve as support of 0D nanomaterials for improving photocatalytic performance, *Appl. Catal. B Environ.* 240 (2019) 153–173.
- [7] J. Yang, H. Miao, J. Jing, Y. Zhu, W. Choi, Photocatalytic activity enhancement of PDI supermolecular via π - π action and energy level adjusting with graphene quantum dots, *Appl. Catal. B Environ.* 281 (2021), 119547.
- [8] J. Li, X. Wu, W. Pan, G. Zhang, H. Chen, Vacancy-rich monolayer BiO_{2-x} as a highly efficient UV, visible, and near-infrared responsive photocatalyst, *Angew. Chem. Int. Ed.* 57 (2018) 491–495.
- [9] Z. Chen, Y. Deng, L. Tang, C. Feng, J. Wang, J. Yu, J. Wang, Z. Liu, H. Zhou, Theoretical and experimental study of full spectrum response Z-scheme 0D/2D Ag₆Si₂O₇/CN photocatalyst with enhanced photocatalytic activities, *Appl. Surf. Sci.* 514 (2020), 145963.
- [10] J. Fu, Q. Xu, J. Low, C. Jiang, J. Yu, Ultrathin 2D/2D WO₃/g-C₃N₄ step-scheme H₂-production photocatalyst, *Appl. Catal. B Environ.* 243 (2019) 556–565.
- [11] Q. Xu, L. Zhang, B. Cheng, J. Fan, J. Yu, S-scheme heterojunction photocatalyst, *Chem* 6 (2020) 1543–1559.
- [12] S. Wageh, A.A. Al-Ghamdi, R. Jafer, X. Li, P. Zhang, A new heterojunction in photocatalysis: S-scheme heterojunction, *Chin. J. Catal.* 42 (2021) 667–669.
- [13] C. Cheng, B. He, J. Fan, B. Cheng, S. Cao, J. Yu, An inorganic/organic S-scheme heterojunction H₂-production photocatalyst and its charge transfer mechanism, *Adv. Mater.* 33 (2021), 2100317.
- [14] Y. Chen, M. Xu, J. Wen, Y. Wan, Q. Zhao, X. Cao, Y. Ding, Z.L. Wang, H. Li, Z. Bian, Selective recovery of precious metals through photocatalysis, *Nat. Sustain.* 4 (2021) 618–626.
- [15] X.-Y. Liu, G. Zhang, H. Chen, H. Li, J. Jiang, Y.-T. Long, Z. Ning, Efficient defect-controlled photocatalytic hydrogen generation based on near-infrared Cu-In-Zn-S quantum dots, *Nano Res.* 11 (2018) 1379–1388.
- [16] F. Kayaci, S. Vempati, I. Donmez, N. Biyikli, T. Uyar, Role of zinc interstitials and oxygen vacancies of ZnO in photocatalysis: a bottom-up approach to control defect density, *Nanoscale* 6 (2014) 10224–10234.
- [17] J. Wang, L. Yu, Z. Wang, W. Wei, K. Wang, X. Wei, Constructing 0D/2D Z-scheme heterojunction of CdS/g-C₃N₄ with enhanced photocatalytic activity for H₂ evolution, *Catal. Lett.* 151 (2021) 3550–3561.
- [18] M. Ou, W. Tu, S. Yin, W. Xing, S. Wu, H. Wang, S. Wan, Q. Zhong, R. Xu, Amino-assisted anchoring of CsPbBr₃ perovskite quantum dots on porous g-C₃N₄ for enhanced photocatalytic CO₂ reduction, *Angew. Chem. Int. Ed.* 57 (2018) 13570–13574.
- [19] L. Wang, Y. Wang, T. Xu, H. Liao, C. Yao, Y. Liu, Z. Li, Z. Chen, D. Pan, L. Sun, M. Wu, Gram-scale synthesis of single-crystalline graphene quantum dots with superior optical properties, *Nat. Commun.* 5 (2014) 5357.
- [20] K.T. Yong, W.C. Law, R. Hu, L. Ye, L. Liu, M.T. Swihart, P.N. Prasad, Nanotoxicity assessment of quantum dots: from cellular to primate studies, *Chem. Soc. Rev.* 42 (2013) 1236–1250.
- [21] J.A. Darr, J. Zhang, N.M. Makwana, X. Weng, Continuous hydrothermal synthesis of inorganic nanoparticles: applications and future directions, *Chem. Rev.* 117 (2017) 11125–11238.
- [22] T. Adschiri, Y.-W. Lee, M. Goto, S. Takami, Green materials synthesis with supercritical water, *Green Chem.* 13 (2011) 1380–1390.
- [23] X. Weng, Q. Zeng, Y. Zhang, F. Dong, Z. Wu, Facile approach for the syntheses of ultrafine TiO₂ nanocrystallites with defects and C heterojunction for photocatalytic water splitting, *ACS Sustain. Chem. Eng.* 4 (2016) 4314–4320.
- [24] X. Weng, Y. Zhang, F. Bi, F. Dong, Z. Wu, J.A. Darr, Thermocatalytic syntheses of highly defective hybrid nano-catalysts for photocatalytic hydrogen evolution, *J. Mater. Chem. A* 5 (2017) 23766–23775.
- [25] P. Niu, L. Zhang, G. Liu, H.-M. Cheng, Graphene-like carbon nitride nanosheets for improved photocatalytic activities, *Adv. Funct. Mater.* 22 (2012) 4763–4770.
- [26] X. Zhang, X. Xie, H. Wang, J. Zhang, B. Pan, Y. Xie, Enhanced photoresponsive ultrathin graphitic-phase C₃N₄ nanosheets for bioimaging, *J. Am. Chem. Soc.* 135 (2013) 18–21.
- [27] G. Kresse, J. Furthmüller, Efficient iterative schemes for ab initio total-energy calculations using a plane-wave basis set, *Phys. Rev. B* 54 (1996) 11169–11186.
- [28] H. Li, J. Shang, Z. Ai, L. Zhang, Efficient visible light nitrogen fixation with bioborn nanosheets of oxygen vacancies on the exposed {001} facets, *J. Am. Chem. Soc.* 137 (2015) 6393–6399.
- [29] M. Guan, C. Xiao, J. Zhang, S. Fan, R. An, Q. Cheng, J. Xie, M. Zhou, B. Ye, Y. Xie, Vacancy associates promoting solar-driven photocatalytic activity of ultrathin bismuth oxychloride nanosheets, *J. Am. Chem. Soc.* 135 (2013) 10411–10417.
- [30] X. Jiang, Y. Zhang, J. Jiang, Y. Rong, Y. Wang, Y. Wu, C. Pan, Characterization of oxygen vacancy associates within hydrogenated TiO₂: a positron annihilation study, *J. Phys. Chem. C* 116 (2012) 22619–22624.
- [31] Z. Huang, Q. Sun, K. Lv, Z. Zhang, M. Li, B. Li, Effect of contact interface between TiO₂ and g-C₃N₄ on the photoreactivity of g-C₃N₄/TiO₂ photocatalyst: (001) vs (101) facets of TiO₂, *Appl. Catal. B Environ.* 164 (2015) 420–427.

- [32] X. Wang, K. Maeda, A. Thomas, K. Takanabe, G. Xin, J.M. Carlsson, K. Domen, M. Antonietti, A metal-free polymeric photocatalyst for hydrogen production from water under visible light, *Nat. Mater.* 8 (2009) 76–80.
- [33] L. Kavan, M. Grätzel, S.E. Gilbert, C. Klemenz, H.J. Scheel, Electrochemical and photoelectrochemical investigation of single-crystal anatase, *J. Am. Chem. Soc.* 118 (1996) 6716–6723.
- [34] L.K. Putri, B.-J. Ng, W.-J. Ong, H.W. Lee, W.S. Chang, S.-P. Chai, Engineering nanoscale p–n junction via the synergetic dual-doping of p-type boron-doped graphene hybridized with n-type oxygen-doped carbon nitride for enhanced photocatalytic hydrogen evolution, *J. Mater. Chem. A* 6 (2018) 3181–3194.
- [35] Z. Hu, G. Liu, X. Chen, Z. Shen, J.C. Yu, Enhancing charge separation in metallic photocatalysts: a case study of the conducting molybdenum dioxide, *Adv. Funct. Mater.* 26 (2016) 4445–4455.
- [36] N. Tian, Y. Zhang, X. Li, K. Xiao, X. Du, F. Dong, G.I.N. Waterhouse, T. Zhang, H. Huang, Precursor-reforming protocol to 3D mesoporous g-C₃N₄ established by ultrathin self-doped nanosheets for superior hydrogen evolution, *Nano Energy* 38 (2017) 72–81.
- [37] Z. Xing, J. Hu, M. Ma, H. Lin, Y. An, Z. Liu, Y. Zhang, J. Li, S. Yang, From one to two: in situ construction of an ultrathin ²D–²D closely bonded heterojunction from a single-phase monolayer nanosheet, *J. Am. Chem. Soc.* 141 (2019) 19715–19727.
- [38] F. He, B. Zhu, B. Cheng, J. Yu, W. Ho, W. Macyk, 2D/2D/0D TiO₂/C₃N₄/Ti₃C₂ MXene composite S-scheme photocatalyst with enhanced CO₂ reduction activity, *Appl. Catal. B Environ.* 272 (2020), 119006.
- [39] P. Xia, S. Cao, B. Zhu, M. Liu, M. Shi, J. Yu, Y. Zhang, Designing a 0D/2D S-scheme heterojunction over polymeric carbon nitride for visible-light photocatalytic inactivation of bacteria, *Angew. Chem. Int. Ed.* 59 (2020) 5218–5225.
- [40] L. Wang, B. Cheng, L. Zhang, J. Yu, In situ irradiated XPS investigation on S-scheme TiO₂@ZnIn₂S₄ photocatalyst for efficient photocatalytic CO₂ reduction, *Small* 17 (41) (2021), 2103447.
- [41] S. Xu, P. Zhou, Z. Zhang, C. Yang, B. Zhang, K. Deng, S. Bottle, H. Zhu, Selective oxidation of 5-hydroxymethylfurfural to 2,5-furandicarboxylic acid using O₂ and a photocatalyst of Co-thiophenopyrazine bonded to g-C₃N₄, *J. Am. Chem. Soc.* 139 (2017) 14775–14782.
- [42] C. Liu, D. Kong, P.C. Hsu, H. Yuan, H.W. Lee, Y. Liu, H. Wang, S. Wang, K. Yan, D. Lin, P.A. Maraccini, K.M. Parker, A.B. Boehm, Y. Cui, Rapid water disinfection using vertically aligned MoS₂ nanofilms and visible light, *Nat. Nanotechnol.* 11 (2016) 1098–1104.
- [43] Q. Xiang, J. Yu, M. Jaroniec, Preparation and enhanced visible-light photocatalytic H₂-production activity of graphene/C₃N₄ composites, *J. Phys. Chem. C* 115 (2011) 7355–7363.
- [44] W.J. Ong, L.L. Tan, Y.H. Ng, S.T. Yong, S.P. Chai, Graphitic carbon nitride (g-C₃N₄)-based photocatalysts for artificial photosynthesis and environmental remediation: are we a step closer to achieving sustainability? *Chem. Rev.* 116 (2016) 7159–7329.
- [45] X. Chen, R. Shi, Q. Chen, Z. Zhang, W. Jiang, Y. Zhu, T. Zhang, Three-dimensional porous g-C₃N₄ for highly efficient photocatalytic overall water splitting, *Nano Energy* 59 (2019) 644–650.
- [46] Z. Lu, L. Zeng, W. Song, Z. Qin, D. Zeng, C. Xie, In situ synthesis of C-TiO₂/g-C₃N₄ heterojunction nanocomposite as highly visible light active photocatalyst originated from effective interfacial charge transfer, *Appl. Catal. B Environ.* 202 (2017) 489–499.
- [47] M.Z. Ge, C.Y. Cao, S.H. Li, Y.X. Tang, L.N. Wang, N. Qi, J.Y. Huang, K.Q. Zhang, S. S. Al-Deyab, Y.K. Lai, In situ plasmonic Ag nanoparticle anchored TiO₂ nanotube arrays as visible-light-driven photocatalysts for enhanced water splitting, *Nanoscale* 8 (2016) 5226–5234.
- [48] M. Wang, D. Zheng, M. Ye, C. Zhang, B. Xu, C. Lin, L. Sun, Z. Lin, One-dimensional densely aligned perovskite-decorated semiconductor heterojunctions with enhanced photocatalytic activity, *Small* 11 (2015) 1436–1442.
- [49] F. Liu, P. Xiao, E. Uchaker, H. He, M. Zhou, X. Zhou, Y. Zhang, A first-principles study of Pt–Ni bimetallic cluster adsorption on the anatase TiO₂ (1 0 1) surface: probing electron effect of Ni in TiO₂ (1 0 1)-bimetallic cluster (Pt–Ni) on the adsorption and dissociation of methanol, *Appl. Surf. Sci.* 315 (2014) 81–89.
- [50] W. Hage, K.R. Liedl, A. Hallbrucker, E. Mayer, Carbonic acid in the gas phase and its astrophysical relevance, *Science* 279 (1998) 1332–1335.
- [51] N.Y. Topsoe, Mechanism of the selective catalytic reduction of nitric oxide by ammonia elucidated by in situ on-line fourier transform infrared spectroscopy, *Science* 265 (1994) 1217–1219.